Check for updates

Methanol steam reforming using In_2O_3/ZrO_2 coated catalytic static mixers (CSMs)

Stephan Kiermaier, [iD] [a] Phillip Nathrath, [iD] [b] Christopher D. Easton, [iD] [c] Mark Greaves, [c] Thomas M. Kohl, [iD] [c] Robert Stöber, [iD] [a] Christian H. Hornung [iD] [c] and Patrick Schühle [iD] *[b]

Methanol is an attractive chemical hydrogen carrier that can provide hydrogen on demand by catalytic steam reforming – an endothermic reaction which requires efficient heat supply to the catalyst. The catalytic static mixer (CSM) technology offers an efficient way to provide sufficient heat and reactant supply to the catalytic center by high thermal conductivity and short diffusion pathways. In this study, an In_2O_3/ZrO_2 catalyst was deposited on highly conductive 3D printed stainless steel scaffolds, reaching uniform and durable coatings. These CSMs were investigated for the methanol steam reforming reaction in a single tube reactor at 330 °C and 350 °C. Their performance was compared to a conventional fixed bed configuration with In_2O_3/ZrO_2 pellet catalysts. The highest overall conversion for the methanol steam reforming, yielding 93%, was achieved using the CSM system at 330 °C, a low feed flow rate of 0.4 mL min^{-1} and a water : MeOH ratio of 1 : 1. The highest CO_2 selectivity of 98% was achieved using the CSM system at 330 °C, a high feed flow rate of 2.0 mL min^{-1} and a water : MeOH ratio of 1 : 2. For most experiments, the CSM results were slightly improved from the corresponding pellet results. Although this effect is believed to be small at the relatively small pipe diameter used herein, it is an indication of the expected superior heat transfer and fluid flow performance of the CSM system over pellets inside of a catalytic reactor.

Introduction

Achieving net zero emissions by 2050, in accordance with the Paris climate agreement, is only possible by avoiding greenhouse gas emissions from burning fossil fuels and replacing their use with renewable energy.[1] In future energy networks, storage, transport and use of large amounts of renewable energy will be conducted in the form of hydrogen at all places, where a direct electrification of the relevant industrial, mobility, transport or heating sector is not possible. One critical challenge to address in a hydrogen-based energy system is the reversible storage of the compound under a high energy density, as, unlike its gravimetric storage density (33.3 kWh kg^{-1}), the volumetric storage density (3 Wh L^{-1}) of hydrogen is low in comparison to other energy carriers.[2,3] Increasing the volumetric densities by means of physical methods in the form of pressurized gas (GH_2) or cryogenic

liquid (LH_2) is a challenging task. It requires new infrastructure while some drawbacks remain as the low energy density of pressurized hydrogen or boil-off losses of cryogenic hydrogen.[4–6]

The chemical storage of hydrogen in liquids or easily liquefiable substances is considered a promising alternative to storing the compound by physical methods.[4,7,8] Here, a liquid or gaseous reactant (*e.g.* CO_2, N_2, or unloaded liquid organic hydrogen carrier (LOHC) molecules) is loaded catalytically with hydrogen to form the respective hydrogen-rich compound (*e.g.* methanol, dimethylether, ammonia or loaded LOHC molecules) in an exothermic reaction. Due to the liquid or easily liquefiable character of the loaded compound, it can be easily stored and transported, and the hydrogen is released at the place and time of hydrogen and energy demand.

Methanol is considered to be a promising hydrogen carrier for future energy systems.[9] The synthesis of the compound from CO_2 and H_2 is already established as an industrial process.[10] Due to its liquid nature, methanol can be stored and transported in the existing (fossil fuel) infrastructure like crude oil cargo vessels, tank wagons or pipelines.[11] A further advantage of methanol, compared to some of the above-mentioned carriers, is its cross-sectoral application. The molecule can simultaneously be used as a

[a] *Forschungszentrum Jülich, Institute for a Sustainable Hydrogen Economy (INW), Marie-Curie-Straße 5, 52428 Jülich, Germany*

[b] *Lehrstuhl für Chemische Reaktionstechnik, Friedrich-Alexander-Universität Erlangen-Nürnberg (FAU), Egerlandstr. 3, D-91058, Erlangen, Germany. E-mail: Patrick.Schuehle@fau.de*

[c] *Commonwealth Scientific and Industrial Research Organisation (CSIRO), Manufacturing, Private Bag 10, Clayton South, Victoria 3169, Australia*

This journal is © The Royal Society of Chemistry 2026

React. Chem. Eng., 2026, **11**, 625–635 | 625

building block for the chemical industry and act as an energy carrier with energy densities comparable to fossil fuels. In its role as a sustainable fuel, methanol can either be utilized to synthesise gasoline or kerosene, or be re-electrified in a direct or indirect methanol fuel cell. For the indirect route, hydrogen is released from the molecule in the methanol steam reforming reaction (MSR).[12,13]

$$CH_3OH + H_2O \rightleftharpoons 3H_2 + CO_2 \quad \Delta_R H^0 = 49 \text{ kJ mol}^{-1}$$

Interestingly, the generated H_2 originates only partially from the carrier itself, with water contributing stoichiometrically one third of the H_2. Consequently, methanol has a comparably high technical hydrogen density (defined by some of us as the mass of released hydrogen per mass of the carrier) of 18.8 wt% (4.9 kWh L^{-1}).[14] If the emerging CO_2 is captured in a closed carbon cycle, the process does not emit greenhouse gases during its energetic use. The MSR reaction is – depending on the catalyst, applied reaction parameters and the general process route – embedded in a network of alternative reaction pathways,[15] such as methanol decomposition.[16]

$$CH_3OH \rightleftharpoons 2H_2 + CO \quad \Delta_R H^0 = 90 \text{ kJ mol}^{-1} \tag{1}$$
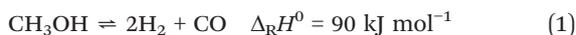
Carbon monoxide can then be consumed as a reactant *via* the water–gas shift (WGS) reaction.

$$CO + H_2O \rightleftharpoons CO_2 + H_2 \quad \Delta_R H^0 = -41 \text{ kJ mol}^{-1} \tag{2}$$

The by-product methane can be formed *via* methanation by either CO_2 or CO hydrogenation.[17,18]

$$CO_2 + 4H_2 \rightleftharpoons CH_4 + 2H_2O \quad \Delta_R H^0 = -247 \text{ kJ mol}^{-1} \tag{3}$$

$$CO + 3H_2 \rightleftharpoons CH_4 + H_2O \quad \Delta_R H^0 = -206 \text{ kJ mol}^{-1} \tag{4}$$

The MSR reaction is usually carried out over Cu, Ni or noble metal catalysts.[15] In_2O_3-based catalysts have emerged as a promising alternative for MSR reactions, and were investigated experimentally and in density functional theory (DFT) calculations.[19–22] These catalysts were shown to provide a high activity over a broad range of temperatures and a high CO_2 selectivity, as CO is effectively oxidized on the reactive lattice oxygens of the In_2O_3 structures.[19,22] In some cases, indium was used as a structural promotor and support during Pd- and Pt-catalyzed MSR reactions.[23–29] Also in the reverse reaction of MSR, namely CO_2 hydrogenation to methanol, In_2O_3-based catalysts have proven to exhibit high activity and stability.[30–34] Monoclinic ZrO_2 is an attractive catalyst support material, as it introduces tensile forces to the In_2O_3 lattices, triggering the formation of a surplus of active oxygen vacancies.[31]

So far, technically relevant MSR studies with In_2O_3/ZrO_2 were conducted using the catalyst in a pellet form in a fixed bed. Pelletised catalysts generally have favourable characteristics for technical realisation, such as a lower pressure drop than a corresponding powder packed bed. However, some other aspects remain issues to address. These include the need to transport sufficient heat and mass through the metal oxide matrix to the catalytically active species in the inner parts of the pellets during endothermic reactions, and the requirement to better control the flow field.[35]

In this study, we present an In_2O_3/ZrO_2 catalyst coated on a catalytic static mixer (CSM). The CSM technology emerged as a means of intensification of chemical processes in recent years. These additively manufactured structures consist of a metal scaffold that can be coated *via* a range of different deposition methods, such as electrodeposition,[36] metal cold spraying[37] and wash coating[38,39] to effect a continuous layer containing the catalytically active species. The metal scaffold provides high mechanical stability for the catalytic coating and a robust solution during manual and mechanical handling; it acts as a flow directing and mixing element and promotes heat transfer in the radial and axial directions. This effect has been well characterized by the Freund group in recent years.[40–42] In contrast to the random nature of a packed bed, the CSM geometry can be specifically designed for a certain fluid application, leading to the flow being well defined and the pressure drop along the length of the CSM being very low.[43] The thin porous catalytic coating can further reduce the diffusion path for reactants, reducing pore diffusion influences compared to a packed bed of catalyst pellets. The recent progress in metal 3D-printing techniques has allowed for complex structures, which will significantly increase the applicability of the CSM technology in catalytic processes.[36]

This study presents the first use of the CSM technology in combination with a novel sol–gel composite based coating protocol of an In_2O_3/ZrO_2 catalyst for the MSR reaction system and compares its performance with the pelletized In_2O_3/ZrO_2 regarding the conversion and selectivity of CO_2, CO and CH_4 formation. By this comparison, we aim to determine if the inherent characteristics of the CSM technology can improve the process efficiency of In_2O_3/ZrO_2-based MSR. Our procedure further provides a blueprint for transferring other catalytic systems to the CSM technology, expanding possible fields of application in which the advantages of CSM technology to increase the efficiency of chemical processes are utilized.

Experimental and methodology

Materials

The catalysts used in this work were prepared using indium nitrate hydrate (Alfa Aesar, Puratronic®, 99.999% metals basis). Cylindrical zirconia oxide pellets with a 3 mm diameter from Thermo Fisher Scientific Pty Ltd were used as a support for the indium oxide phase. Disperal from Sasol Ltd was used as a binding agent. The reactant methanol was purchased from Merck Inc (LiChrosolv methanol for liquid chromatography).

626 | *React. Chem. Eng.*, 2026, **11**, 625–635

This journal is © The Royal Society of Chemistry 2026

CSM and catalyst preparation and characterization

3D printing of the scaffold. The static mixer scaffolds were manufactured using powder bed direct metal 3D printing. They were supplied by Precision Catalysts (https://precisioncatalysts.com.au/) and made from 316L stainless steel powder; the design and method are described in previous work.[37] Each mixer had a total length of 250 mm, a diameter of 10 mm and a void fraction of 75%. The mixer design used was a diamond cut lattice, which is an effective mixing geometry for biphasic flow. This mixing lattice design with tube diameters ranging from 6 mm to 29 mm ID was used various gas–liquid and gas phase processes, including similar highly endothermic reactions, like the release of hydrogen from organic hydrogen carriers (*e.g.* dehydrogenation of methyl cyclohexane).[37,44]

Catalysts. The pelletised In_2O_3/ZrO_2 catalysts were synthesized using a wet impregnation approach as described by Stöber *et al.*[35] To provide the catalytic coating of the CSM structures, zirconium oxide pellets were milled in a ring mill for 4 min at 200 rpm and subsequently shaken overnight with 2 mm zirconia beads. A Malvern Mastersizer with a sample suspension unit was used to ensure that the final particle size was sufficiently small ($d_{50} < 1$ μm, $d_{90} < 2$ μm) for the coating procedure. The catalytically active coating was prepared analogously to the methodology as described in our previous work, investigating the coating of steel plates for the dehydrogenation of perhydro-benzyltoluene.[45,46] In this procedure, a sol–gel composite approach is used in which a sol–gel acts as an inorganic binder in combination with a filler component (in our case zirconia powder).

The sol is prepared by dispersing both indium nitrate and the precursor Disperal (AlOOH/boehmite) in a mixture of water and HNO_3. The milled carrier component ZrO_2 is then added to the sol, and the aging process is started while stirring at 1000 rpm. The dispersion recipe used for the coating in this work is shown in Table 1.

Dip coating. A dip coating technique was chosen to coat the CSM with the catalytically active species. In contrast to techniques like spray-coating that would only allow the coating of areas that can be reached by a spray nozzle, dip coating enables a uniform impregnation of the inner voids of the 3D scaffold structure. Prior to coating, the CSM was cleaned *via* three subsequent ultrasonication steps of 10 min each in a 1 wt% HCl solution, acetone and deionized water. After an aging time of 4 h, the sol–gel was filled into a 20 mL cylinder. The CSM was then dipped twice into the sol–gel for one minute each, to achieve sufficient coverage and catalyst

Table 1 Dispersion recipe for the dip coating of the catalytic static mixers

Zirconia	$m_{ZrO_2} = 21.667$ g
Indium	$m_{In(NO_3)_3 \cdot H_2O} = 2.068$ g (indium-content: 3 wt%)
Binder	$m_{AlOOH/boehmite} = 2.4074$ g ($m_{Binder}:m_{carrier} = 1:9$)
Nitric acid	$m_{HNO_3} = 2.4074$ g ($m_{HNO_3}:m_{carrier} = 1:9$)
Conditions	T = room temperature, $n_{stirrer} = 1000$ rpm, $t_{aging} = 4$ h

Table 2 Temperature profile for the calcination of the coated CSM

Temperature/°C	Rate/K min^{-1}	Holding time/h
100	1	0.5
550	2	6
Room temperature	30	—

loading of the CSM scaffold. Afterwards, the CSM was dried under ambient conditions overnight. The coated and dried CSMs were then calcined using the program described in Table 2.

The remaining sol–gel after the dip coating process was also calcined and analysed. Mechanical stability tests of the coated CSMs were carried out with a Bandelin Sonorex Digitec DT 514 BH.

Analysis of chemical composition and total surface. Determination of the elemental composition of the coating was carried out *via* ICP measurement with an Agilent 5900 ICP-OES. The pore size of the coating was analysed with an Autosorb iQ Station 2 from Quantachrome Instruments.

Imaging. A virgin CSM test piece (2 cm) was prepared analogously to the CSMs to be tested in the reaction and then examined *via* scanning electron microscopy (SEM) and X-ray photoelectron spectroscopy (XPS). Images were taken using a Zeiss Merlin FESEM at an accelerating voltage of 5 kV in the secondary electron or in-lens modes depending on magnification. The test samples were mounted on aluminium stubs using carbon tape. The samples were coated with conductive iridium using a Cressington 208HR sputter coater for 30 s to give approximately a 4 nm coating. Energy Dispersive X-Ray Spectroscopy (EDXS) was used to determine the elemental composition, using an Oxford Instruments X-Max 80 mm^2 SSD detector at an accelerating voltage for SEM of 30 kV.

Further information on the elemental composition of the final coating was acquired *via* X-ray photoelectron spectroscopy (XPS). For this purpose, an additional 2 cm CSM test piece was embedded in a resin, cut and polished with a diamond paste successively down to 1 μm in a transverse axis. The sample was sonicated in a solution of 2% RBS 35/2% ethanol in MilliQ prior to its loading into the instrument. Additional cleaning was performed *in situ* using an Ar^+ ion source (Minibeam 6 – Kratos) to remove the resin remaining on the surface. XPS analysis was performed using an AXIS Nova spectrometer (Kratos Analytical Inc., Manchester, UK) with a monochromated Al Kα source at a power of 180 W (15 kV × 12 mA) and a hemispherical analyser operating in the fixed analyser transmission mode. The total pressure in the main vacuum chamber during analysis was typically between 10^{-9} and 10^{-8} mbar. XPS imaging was performed for the In $3d_{5/2}$ and Zr $3d_{5/2}$ photopeaks using the method defined in the ESCApe software that removes both the pre- and post-peak backgrounds. Using a combination of XPS and optical imaging, specific areas representing the CSM, coating and resin were selected for small spot analysis. Survey spectra were acquired at a pass energy of 160 eV and a step size of 0.5 eV in FOV2 lens mode and a 55 μm aperture (analysis area: roughly double the aperture size). Data processing was

This journal is © The Royal Society of Chemistry 2026

React. Chem. Eng., 2026, **11**, 625–635 | **627**

performed using CasaXPS processing software version 2.3.26 (Casa Software Ltd., Teignmouth, UK). All elements present were identified from the survey spectra. The atomic concentrations of the detected elements were calculated using integral peak intensities and the sensitivity factors supplied by the manufacturer. These values were converted to wt% using the conversion calculator hosted on the XPS fitting webpage.[47]

Setup and experimental procedure for the methanol steam reforming experiments

Setup. The reactor was either packed with two CSMs or with a diluted fixed bed consisting of the pelletized catalyst (pellet dimensions: $d = 3.25 \pm 0.08$ mm, $l = 5.01 \pm 0.94$) and glass Raschig rings (Raschig ring dimensions: 3 mm diameter and 8 mm average length). In the latter case, the size and, consequently, the bulk density of the mixture containing the pelletized catalysts were adjusted to create a similar gas space within the system as in the CSM experiments, ensuring comparable residence times in the reactor.

The steam reforming reaction is carried out in a Black Sapphire flow reactor from the company Precision Catalysts. The tubular reactor has a total length of 700 mm and an inner diameter of 10 mm. We set the active catalytic length inside the reactor, for both, the CSM and the pellet tests, to a maximum of 500 mm, which equates to two 250 mm long CSMs in series. The catalytic zone is fully contained within the heated section of the reactor. Temperature control is carried out *via* three thermocouples that are located along the length axis of the reactor mantle. After the condensation of non-converted reactants, a Shimadzu GC-2010 Plus model equipped with a BID-2010 Plus detector was used for offline analysis of the permanent gases (H_2, CO_2, CO and CH_4). A flow scheme of the reactor with further details of the experimental setup can be found in the SI.

Experimental procedure. Prior to an experiment, the reactor was purged with nitrogen under atmospheric pressure to remove air. Under flowing nitrogen, the reactor was heated to the desired temperature and the pressure increased. After reaching the set temperature, the desired mass flow of the water–methanol mixture was adjusted using a Vapourtec SF-10 peristaltic pump. The product gas composition was regularly checked *via* offline GC measurements to assess whether the system is in steady-state operation. The occurrence of continuous gas compositions marked a new set experimental point at the respective set parameters. The customized method for the analysis of gaseous samples in the offline GC can be found in the SI. An overview of all examined set points, as well as reproduced experiments, is shown in the SI Tables S3–S6.

Results

Chemical and morphological properties of the coated CSMs

Uniformity & mechanical durability. The dispersion recipe that was developed in this work aimed at the synthesis of a coating that easily penetrated the inner structure of the CSMs
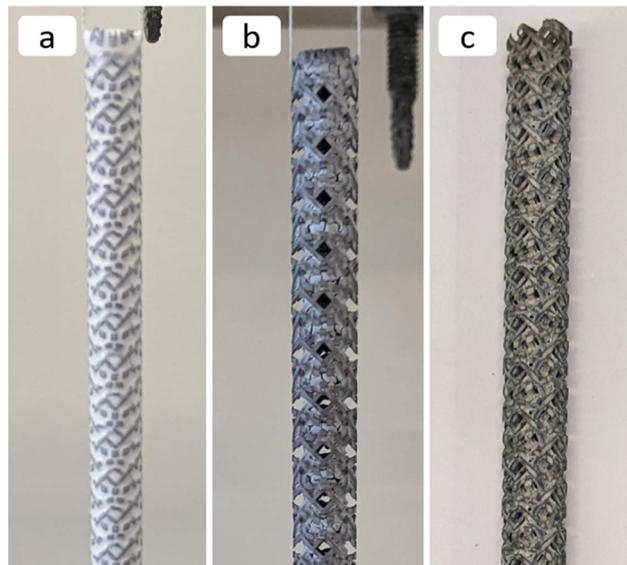

Fig. 1 Pictures of a CSM after dipping twice (a), after drying overnight (b) and after the calcination procedure (c).

and at the same time adhered well to the CSM scaffold surface so that a sufficient amount of coating is deposited homogeneously. Fig. 1 shows a CSM that was coated twice (a), then dried overnight (b) and the CSM after the calcination procedure (c).

Dip coating of the CSMs resulted in a uniform coating after drying overnight. Mechanical durability of the coating was evaluated in an ultrasonication stress test. The losses of the CSM coating in three subsequent 10 min ultrasonication intervals with 860 W power and at 35 kHz frequency was below 1 wt% after each run.

Composition and total surface. To analyse the elemental composition and morphological surface structure of the coating, the left-over sol–gel composite dispersion from the dip coating process was calcined and analysed. The elemental composition as determined *via* ICP-OES and BET surface area calculated from N_2-physisorption are shown in Table 3 (extended data are available in Table S2 of the SI).

Detailed structure and composition analysis. The morphological microstructure of the coating was analysed *via* SEM and SEM-EDXS. Three spots of different surface structures that were observed during the SEM investigations and an SEM-EDXS image of a spot showing the CSM scaffold and the In_2O_3/ZrO_2 coating are shown in Fig. 2. Further images can be found in the SI.

The SEM analysis showed that large parts of the CSMs were evenly coated with the In_2O_3/ZrO_2 catalyst (Fig. 2a-1–a-3). The details of the SEM pictures (Fig. 2a-3) revealed structures in the sub-micron to micron range on the surface that probably represent zirconia powder particles which have agglomerated during calcination. The outer side of the CSM showed some small areas in the one-to-two-digit micron range that were not covered with the coating (Fig. 2b-1–b-3; highlighted with white boxes in Fig. 2b-2). The less uniform coating of the outer parts

628 | *React. Chem. Eng.*, 2026, **11**, 625–635

This journal is © The Royal Society of Chemistry 2026

Table 3 Elemental composition determined by ICP-OES and BET surface area calculated from N_2-physisorption

	In/wt%	Al/wt%	Zr/wt%	BET surface area/m^2 g^{-1}
In_2O_3/ZrO_2 on CSM – 1st layer	3.13	1.25	60.1	55.4
In_2O_3/ZrO_2 on CSM – 2nd layer	3.29	1.10	61.4	55.4
In_2O_3/ZrO_2 pellet catalyst	3.03	0.33	65.4	96.6
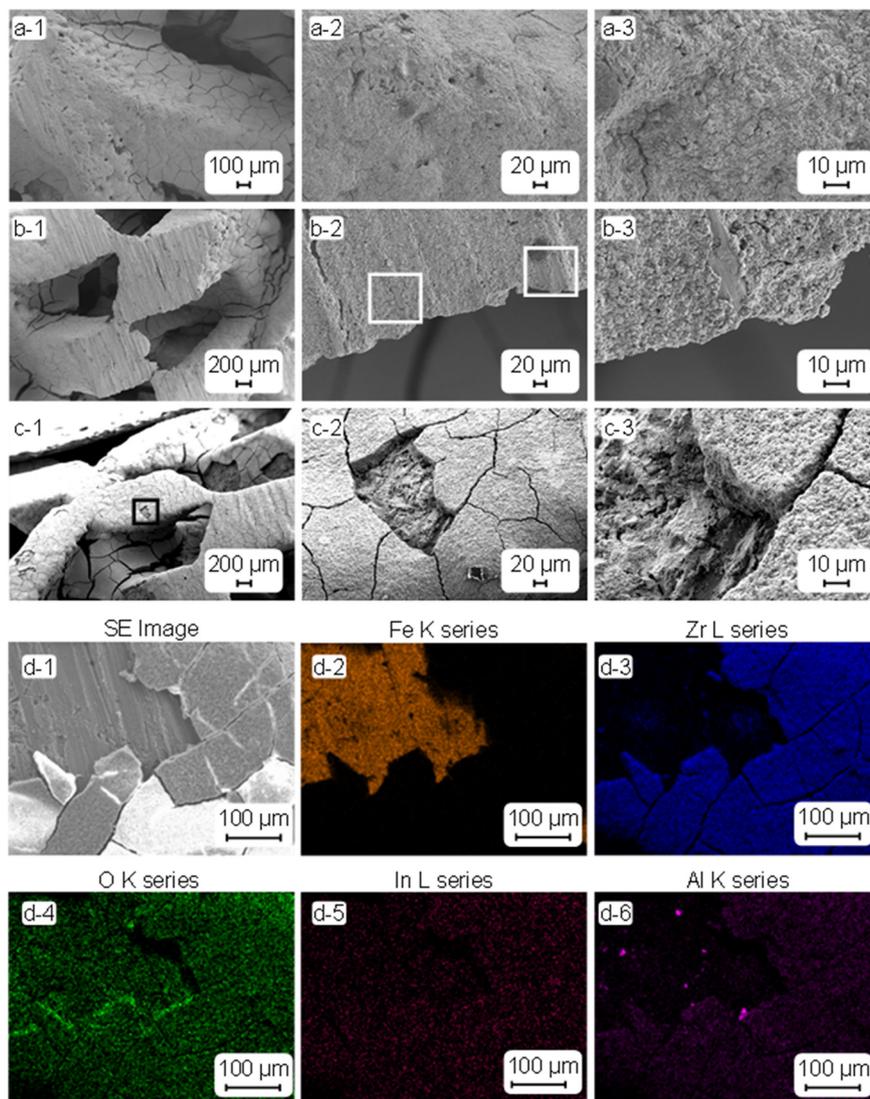
Fig. 2 SEM images showing an evenly coated surface (a), uncoated spots on the outer region of the CSM (b), and cracks and small defects of the coating (c) and SEM-EDXS images (d2–d6 show different elements) of a spot showing the CSM scaffold and the In_2O_3/ZrO_2 coating (d). Images 1–3 in the rows a–c show the microscopic images at different scales.

of the CSM is a result of faster solvent evaporation in this region during overnight drying, forcing the dispersion into the inner parts of the CSM where drying is slower. Furthermore, excess dispersion can run down the CSM outside but is held in place by surface tension in the inner voids of the CSM. The coating showed some cracks and minor defects (Fig. 2c-1–c-3). These irregularities are a result of the calcination process in which the fast evaporation of water as well as the difference in thermal extension of the metal substrate and ceramic coating can lead

to cracks or even spalling or chipping of the coating. Despite the optical defects, the In_2O_3/ZrO_2 coating had a high mechanical stability as demonstrated by the ultrasonication stress test. This indicates a durable mechanical interlinking of the coating layer and the metal substrate. The SEM data of the detail (Fig. 2c-3) shows no bare stainless steel at the inner parts of the defects at the magnifications used, indicating adherence of the coating on the substrate. Further optimization to reduce cracks or defects could be achieved by decreasing the water

This journal is © The Royal Society of Chemistry 2026

React. Chem. Eng., 2026, **11**, 625–635 | **629**

content in the coating or slower temperature ramp during heating and cooling on the calcination oven. Also, adjusting the dip coating recipe in a way that results in thinner layers could reduce cracks or defects but would require more dip coating steps to achieve the same amount of catalyst on the CSM.

For SEM-EDXS mapping, a detailed image of the CSM was chosen that showed both the CSM scaffold and catalytic coating with cracks (Fig. 2d-1–d-6). The 316L stainless steel scaffold of the CSM clearly showed the main component iron (Fig. 2d-2) while signals from the coating came largely from zirconium (Fig. 2d-3). Interestingly, oxygen was detected in the coating as expected, but also on the uncoated parts of the CSM (Fig. 2d-4). While clarification of this finding requires further research, our suggestion is that the acid treatment of the bare CSM scaffold during the pre-treatment procedure could have resulted in a partial oxidation of the material. Note further that the detector we used was adjusted to enhance the probability of detecting Zr with high accuracy. Thus, the oxygen detection in our images was not optimized to the highest possible sensitivity to clearly detect differences in oxygen contents within the area investigated. Indium was probably at the lower detection limit of the device, and hence no clear distinction between the CSM and coating was possible in this case (Fig. 2d-5). Aluminum was detected in the coating what was attributed to alumina that was present as a binder in the coating recipe (Fig. 2d-6). Some smaller particles rich in the binder derived Al or minor Al contaminations can also be detected sitting on top of the bare CSM.

For sufficiently accurate detection of indium in the coating, XPS small spot analysis of a cross-section of an additional 2 cm CSM test piece was carried out. Optical images, taken outside of the instrument with a camera (Fig. 3a-1) and taken with the camera located in the instrument (Fig. 3a-2), XPS images of indium and zirconia and the elemental composition (wt%) derived from the survey spectra are depicted in Fig. 3. Further information and the employed method are provided in the experimental and methodology section.

The optical investigation of the cut test piece showed that the coating had successfully penetrated into the inner parts of the CSM framework (Fig. 3a-1 and a-2). The XPS imaging resulted in clear signals for indium (Fig. 3b-1) and zirconium (Fig. 3b-2) in the coating of the CSM. A quantitative comparison of the oxygen, zirconium, indium and aluminium signals resulted in an average surface indium content of $w_{In,coating}$ = 3.2 wt% which corresponds well with the results from ICP analysis (see Table 3).

Comparison of the In$_2$O$_3$/ZrO$_2$ coated CSMs and fixed bed configuration in methanol steam reforming

Our experimental campaign aimed at comparing the performance of the CSMs with the same catalyst in pellet form
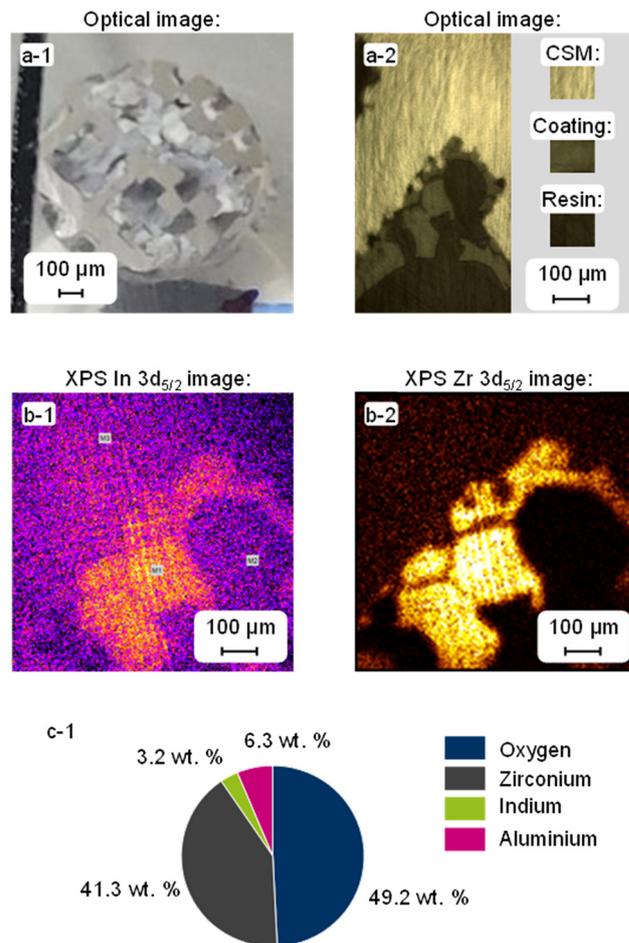

Fig. 3 Optical images, taken outside of the instrument with a camera (a-1) and taken with the camera located in the instrument (a-2); XPS images of indium (b-1) and zirconia (b-2) and the calculated composition (wt%) from the XPS small spot point analysis of the coating (c-1).

used in a fixed bed. To achieve comparable results, we used the same amount of indium (0.3875 g, corresponding to a total of 12 g of catalyst) and the same CSM/catalyst bed length. We further ensured the same residence times by adjusting the void fraction in the reactor in the two series of experiments with either CSMs or the pelletised catalyst (see Experimental and methodology). The MSR experiments were performed with molar feed ratios of 1:1 and 2:1 ($n_{H_2O}:n_{MeOH}$) and varying reactant flows between 0.4 mL min^{-1} and 2.0 mL min^{-1}. The CSMs and fixed bed were both tested at 330 °C and 350 °C as the indium-based catalytic system is known to be active in this temperature region.[35]

Methanol steam reforming with a molar feed ratio of 1:1 ($n_{H_2O}:n_{MeOH}$)

The first experiments were carried out with a molar water to methanol feed ratio of 1:1. The calculated conversion of methanol and the respective selectivities to CO$_2$ at 330 °C and 350 °C using the CSM and the fixed bed pellet catalyst are shown in Fig. 4.
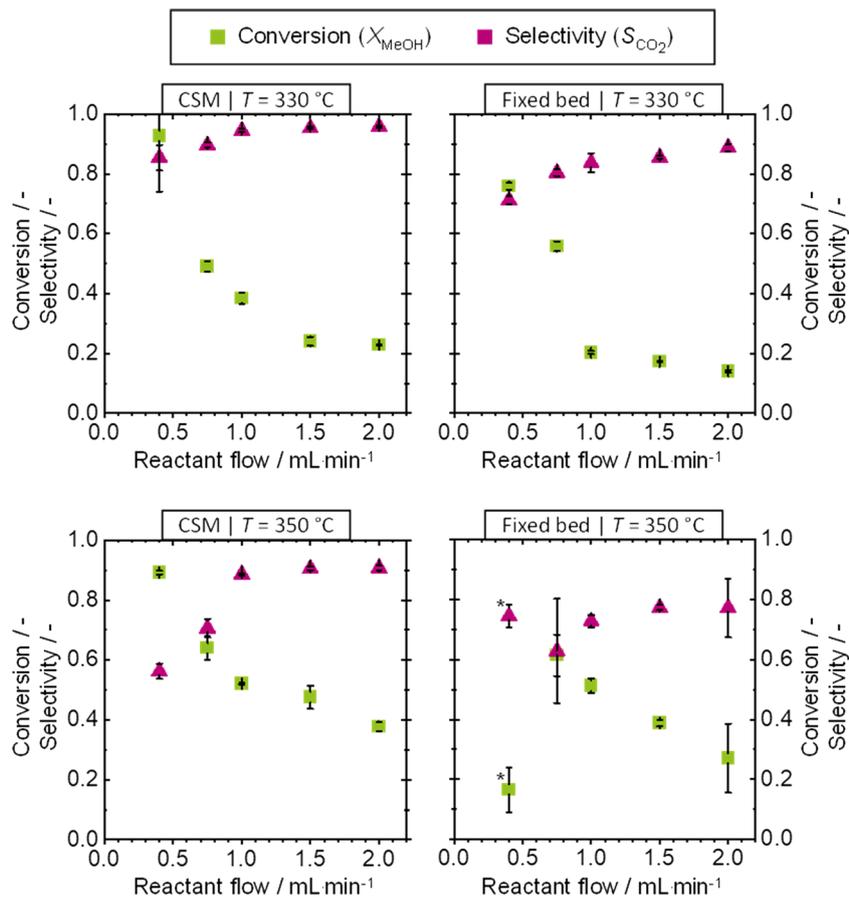
Fig. 4 Conversion and selectivity of the methanol steam reforming reaction with a molar ratio of water to methanol of $1:1$ at 330 °C (top) and 350 °C (bottom) with the catalytic static mixer (CSM) technology (left) and a fixed bed (right), respectively. Experimental conditions: T = 330 °C (top)/350 °C (bottom), p = 2 bar_a, m_{In} = 0.3875 g, $\dot{n}_{H_2O} : \dot{n}_{MeOH}$ = $1:1$. Catalysts: In_2O_3/ZrO_2 3 wt% CSM (left) and pellets in a fixed bed (right).

Conversion. The methanol conversions (calculated on carbon basis) were on average higher at 350 °C for both CSMs and pellets than at 330 °C. The highest conversions of 93% (T = 330 °C) and 89% (T = 350 °C) were detected with the CSM system at the lowest reactant flow of 0.4 mL min^{-1}. An increasing reactant flow led to a decrease of the conversion to a minimum of 23% (T = 330 °C) and 38% (T = 350 °C) with the CSM system at 2.0 mL min^{-1}. The decreasing conversion at higher flow rates are a result of the shorter residence times in the reactor. With the fixed bed catalyst, the conversions were slightly lower ranging from 76% at 0.4 mL min^{-1} to 14% at 2.0 mL min^{-1} (T = 330 °C) and from 61% at 0.8 mL min^{-1} to 26% at 2.0 mL min^{-1} (T = 350 °C).

An outstanding operating point was observed with the pellet catalyst at the lowest volume flow of 0.4 mL min^{-1} at 350 °C (marked with * in Fig. 4). Following the general trend of the other experiments, the highest conversion of the pellet catalyst is expected at this temperature, but only 17% conversion was measured. This phenomenon hints that other influencing factors have occurred at the operating point. This phenomenon occurred only at the fixed bed benchmark and at an operating point which is considered unstable and which has a low reproducibility due to the low reactant

rate. Consequently, it was deemed to be of low significance and the authors decided against elucidating this effect in detail. An extended discussion of this phenomenon can be found in the SI.

The MSR generally requires i) the presence of the two reactants, methanol and water, at the reactive site *via* convective and diffusive mass transport and ii) heat provision at the catalytic center for the endothermic reaction to occur. It is tempting to explain the small but noticeable differences in performance between the two catalysts with improved mass and/or heat transport, which are attributed to CSMs and similar structures compared to pellet catalysts in the literature.[37,41,44,48] Therefore, the following discussion will give some insight into the probable influence of transport phenomena.

Mass transport. A sufficient supply (high surface concentration) of reactants at the catalytic site is determined in both heterogeneous systems by diffusive and convective processes. While the convective bulk flow is defined and set *via* the reactant flow, diffusive flows with the CSM system and the pelletized catalyst are determined by the lengths of diffusive pathways and the porosity of the catalytic system.

BET measurements have shown that the pellet catalyst has a larger surface area (96.6 m^2 g^{-1}) in contrast to the coating

on the static mixers (55.4 m^2 g^{-1}). However, the two systems differ much more with regard to their geometrical dimensions. The catalyst support material thickness, which influences the length of the diffusion paths of the reactants, was between approx. 50 and 200 μm at the CSMs, while the pellet catalyst support has a diameter of 3.25 mm. Further, as described above, the active layer of the CSM consists of agglomerated zirconia particles in the micron to sub-micron range. This hints at the existence of an easily accessible channel system between the particles with larger pores than those of the zirconia pellets (a mean pore diameter of 20 nm). With those favorable CSM characteristics in mind, the Weisz–Prater criterion was calculated to determine if internal mass transport influences the MSR with the pellet and/or CSM catalysts (for details see the SI). While the resulting value for the CSM (~0.01) is about one-to-two orders of magnitude lower than the value for the pellets (~0.5), neither exceed the threshold of 1.0. Therefore, no mass transport limitations are expected under the applied reaction conditions, which match well with the observed, small differences between the two catalyst conversions. However, this trend indicates that with elevated reaction temperatures (e.g. 400 °C), which will be necessary to achieve full methanol conversion at reasonable reactant flows, pore diffusion will dominate the MSR over the pellet catalyst and in turn give the CSMs an advantage.

Heat provision. The coated CSM and the pellet catalyst differ significantly in their material composition. This leads to differences in their effective heat conductivity. By using the CSM technology, the reaction volume, i.e. the inner part of the tube with the dimensions of 10 mm diameter and 500 mm total length, consists of 25% of 316L stainless steel with a high heat conductivity of approx. 13–18 W m^{-1} K^{-1}. In our experimental series with the pellet catalyst, the reaction volume consisted predominantly of glass rings (approx. 1 W m^{-1} K^{-1}) and the catalyst carrier zirconia (approx. 1.6 W m^{-1} K^{-1}). Thus, the increased observable activity of the CSMs could be resulting from improved heat transfer through the solid metal scaffold, which is conducting heat, provided through the outer tube wall, in both the radial and axial directions. It should be noted that meaningful improvements in reaction performance from such an enhanced heat transfer are expected to occur at reactor diameters significantly larger than the 10 mm ID tube used in our laboratory experimental rig. For example, in previous work we have modeled this effect for endothermic LOHC dehydrogenation in a tube with 50 mm ID and observed a very noticeable difference in temperature profiles between a structured catalyst and a packed bed, while there was only a minimal difference at 6 mm ID under comparable conditions.[49] As a next step, we will transfer this novel coating protocol to larger CSM structures, which will allow for extended reaction engineering studies, specifically including measurements of radial and axial temperature profiles; such measurements were not feasible in our 10 mm system due to space constraints.

Selectivity. The CO$_2$ selectivities at different temperatures and flow rates with the CSM and the fixed bed configuration are shown in Fig. 4. A detailed presentation of the formed by-products of methane and carbon monoxide, as well as a brief assessment of catalyst stability in a continuous reaction, can be found in the SI. Apart from forming desired products H$_2$ and CO$_2$, the MSR can be accompanied by methanol decomposition, forming CO. Further, hydrogenation of the carbon-based products (CO$_2$ or CO) of both reactions can result in the formation of methane. CO, CO$_2$, H$_2$O and H$_2$ are further linked by the (reverse) water–gas-shift reaction. The offline analytics that were used allowed for the detection of the permanent gases H$_2$, CO$_2$, CO and CH$_4$, which were all detected during the experiments.

The CO$_2$ selectivities display a pronounced dependency on the conversion level and the volume flow of the reactants in regards to their residence time at both temperatures. This phenomenon is due to the fact that high conversions result in higher CO$_2$ and simultaneously lower water partial pressures, which in turn promote conversion of CO$_2$ to CO via the reverse water–gas-shift reaction. This is especially pronounced at low flow rates, where decreased CO$_2$ selectivities can be detected. Furthermore, the water–gas-shift reaction is thermodynamically favored at lower temperatures, leading to higher CO$_2$ selectivities at 330 °C with both catalyst technologies. Again, the CSMs reach slightly higher CO$_2$ selectivities compared to the fixed bed at all temperatures and flowrates. In addition, the operating point at 0.4 mL min^{-1} and 350 °C with the fixed bed differed again remarkably from the expected trend, which should be discussed in following future investigations.

Methanol steam reforming with a molar feed ratio of 2:1 ($n_{H_2O} : n_{MeOH}$)

Conversion. The detected conversions at a molar feed ratio of water and methanol of 2:1 (see Fig. 5) follow the same trend as was observed at a ratio of 1:1 (see Fig. 4). An increase of the reactant flow leads to lower overall conversions due to the shorter residence times of the reactants within the reactor. The highest conversions of 87% (T = 330 °C) and 88% (T = 350 °C) were detected with the CSM system at the lowest reactant flows. The respective conversions of the CSM and pellet catalysts were on average comparable to the performances achieved at a water and methanol ratio of 1:1. Again, the conversion at the lowest reactant volume flow resulted in an unexpected low conversion which needs to be addressed in future investigations looking at these specific operating points at the edge of our current operating window in more detail.

Selectivity. Increasing the molar ratio of water to methanol by a factor of two showed a similar trend of rising CO$_2$ selectivity at increased reactant flows and low conversions. The detected selectivities, however, were generally higher in comparison to feeding the reactants in a

632 | React. Chem. Eng., 2026, **11**, 625–635

This journal is © The Royal Society of Chemistry 2026
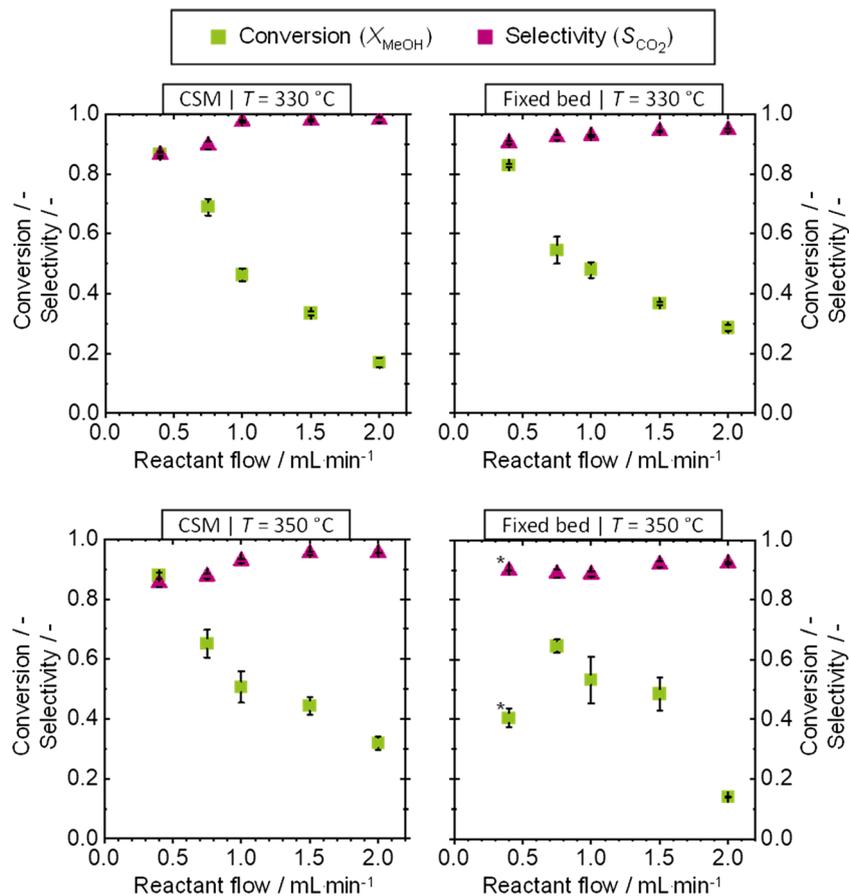
Fig. 5 Conversion and selectivity of the methanol steam reforming reaction with a molar ratio of water to methanol of 2:1 at 330 °C (top) and 350 °C (bottom) with the catalytic static mixer (CSM) technology (left) and a fixed bed (right), respectively. Experimental conditions: T = 330 °C (top)/350 °C (bottom), p = 2 bar$_a$, m_{In} = 0.3875 g, $\dot{n}_{H_2O} : \dot{n}_{MeOH}$ = 2:1. Catalysts: In$_2$O$_3$/ZrO$_2$ 3 wt% CSM (left) and pellets in a fixed bed (right).

molar ratio of 1:1. The higher selectivities can be traced back to the higher H_2O vapor pressures in the system, which suppress the water–gas-shift reaction and subsequent reactions of CO to further by-products. Increasing the water content in the system thus shows a technically feasible method of achieving high CO_2 selectivities. In a technical process, evaporating and condensing the surplus water would demand an additional energy input. If the additional energy costs for the evaporation of this surplus water were not to be considered, then other means of increasing reactant partial pressure and decreasing product partial pressures could be warranted, such as additional feed of reactants along the reactor length or an integrated removal of products *via* membranes. Furthermore, the high selectivities at high reactant flows come with the cost of low conversions and thus low reactant consumption and the need to separate unreacted compounds from products downstream of the reactor in a technical scenario. An optimum operating point is therefore a combination of reactor temperature and reactant flows where conversions are high, while the decrease of selectivity due to the high CO_2 concentration and subsequent CO formation resulting from the water–gas-shift reaction is still acceptable.

Conclusion

In this work, we have successfully developed a new In_2O_3/ZrO_2 coating that was used as a catalytically active layer on CSMs and tested in the MSR reaction. Synthesis of the catalytic coating was carried out by preparing a sol–gel containing zirconia, indium and a binder. Two coating layers were then applied *via* a dip coating procedure followed by a calcination procedure to yield the active species.

Stress tests showed that the two layers adhere sufficiently to the stainless steel scaffold. SEM imaging of the coating revealed a uniform coating thickness with small defects. ICP, SEM-EDXS and XPS analysis showed consistently that the coating contained 3 wt% In as intended in the sol–gel recipe.

For most experiments, the conversions achieved using the CSMs were slightly improved from corresponding pellet catalyst runs – an early indication that improved heat and mass transfer, using these structured 3D printed catalysts, is expected to result in superior performance on a technically relevant scale. The selectivities to CO_2 were high at high volume flows and low conversions as the methanol concentration over the reactor length was high at these operating points. At high conversions, high CO_2 concentrations and decreased water partial pressure

This journal is © The Royal Society of Chemistry 2026

React. Chem. Eng., 2026, **11**, 625–635 | **633**

in the reactor resulted in the formation of CO *via* the reverse water–gas-shift reaction. Our experimental campaign hinted that the pellet catalyst was subjected to external mass transport effects whereas the CSM system was less prone to limitations by mass transport.

Our application provides a blueprint for transferring other catalytic systems to the CSM technology expanding possible fields of application that can be used to increase the efficiency of chemical processes in which the advantages of CSM technology (defined flow fields or superb heat conductivity) are utilized.

Conflicts of interest

There are no conflicts to declare.

Data availability

Data for this article, including raw data in a machine readable format, are available at Zenodo at DOI https://doi.org/10.5281/zenodo.16569478.

Supplementary information (SI) is available. See DOI: https://doi.org/10.1039/d5re00391a.

Acknowledgements

Notes and references

1 J. Rogelj, D. Shindell, K. Jiang, S. Fifita, P. Forster, V. Ginzburg, C. Handa, H. Kheshgi, S. Kobayashi and E. Kriegler, *Global Warming of 1.5 °C*, An IPCC Special Report on the impacts of global warming of 1.5 °C above pre-industrial levels and related global greenhouse gas emission pathways, in the context of strengthening the global response to the threat of climate change, sustainable development, and efforts to eradicate poverty, 2018.

2 B. Elvers and G. Bellussi, *Ullmann's Encyclopedia of Industrial Chemistry*, Wiley-VCH Verlag GmbH, 2011.

3 B. Elvers, *Ullmann's energy: Resources, processes, products*, Wiley, Hamburg, Germany, 2017.

4 P. Preuster, A. Alekseev and P. Wasserscheid, *Annu. Rev. Chem. Biomol. Eng.*, 2017, **8**, 445–471.

5 A. Züttel, *Naturwissenschaften*, 2004, **91**, 157–172.

6 A. F. Dalebrook, W. Gan, M. Grasemann, S. Moret and G. Laurenczy, *Chem. Commun.*, 2013, **49**, 8735–8751.

7 J. Andersson and S. Grönkvist, *Int. J. Hydrogen Energy*, 2019, **44**, 11901–11919.

8 H. Kim, A. Kim, M. Byun and H. Lim, *Renewable Energy*, 2021, **180**, 552–559.

9 G. A. Olah, *Angew. Chem., Int. Ed.*, 2005, **44**, 2636–2639.

10 D. S. Marlin, E. Sarron and Ó. Sigurbjörnsson, *Front. Chem.*, 2018, **6**, 446.

11 J. Cui and M. Aziz, *Int. J. Hydrogen Energy*, 2023, **48**, 15737–15747.

12 P. Schmidt, V. Batteiger, A. Roth, W. Weindorf and T. Raksha, *Chem. Ing. Tech.*, 2018, **90**, 127–140.

13 S. Schemme, J. L. Breuer, M. Köller, S. Meschede, F. Walman, R. C. Samsun, R. Peters and D. Stolten, *Int. J. Hydrogen Energy*, 2020, **45**, 5395–5414.

14 P. Schühle, R. Stöber, M. Semmel, A. Schaadt, R. Szolak, S. Thill, M. Alders, C. Hebling, P. Wasserscheid and O. Salem, *Energy Environ. Sci.*, 2023, **16**, 3002–3013.

15 M. Rostami, A. H. Farajollahi, R. Amirkhani and M. E. Farshchi, *AIP Adv.*, 2023, **13**(3), DOI: 10.1063/5.0137706.

16 R. Thattarathody, M. Artoul, R. M. Digilov and M. Sheintuch, *Ind. Eng. Chem. Res.*, 2018, **57**, 3175–3186.

17 S. S. Y. Lin, W. J. Thomson, T. J. Hagensen and S. Y. Ha, *Appl. Catal., A*, 2007, **318**, 121–127.

18 W. Wei and G. Jinlong, *Front. Chem. Sci. Eng.*, 2011, **5**, 2–10.

19 H. Lorenz, W. Jochum, B. Klötzer, M. Stöger-Pollach, S. Schwarz, K. Pfaller and S. Penner, *Appl. Catal., A*, 2008, **347**, 34–42.

20 S. Lin and D. Xie, *Chin. J. Chem.*, 2012, **30**, 2036–2040.

21 E.-M. Köck, M. Kogler, M. Grünbacher, C. Zhuo, R. Thalinger, D. Schmidmair, L. Schlicker, A. Gurlo and S. Penner, *J. Phys. Chem. C*, 2016, **120**, 15272–15281.

22 J. Wang, H. Wang and P. Hu, *Sci. China: Chem.*, 2018, **61**, 336–343.

23 N. Iwasa and N. Takezawa, *Top. Catal.*, 2003, **22**, 215–224.

24 R. L. Barbosa, V. Papaefthimiou, Y. T. Law, D. Teschner, M. Hävecker, A. Knop-Gericke, R. Zapf, G. Kolb, R. Schlögl and S. Zafeiratos, *J. Phys. Chem. C*, 2013, **117**, 6143–6150.

25 D. Liu, Y. Men, J. Wang, G. Kolb, X. Liu, Y. Wang and Q. Sun, *Int. J. Hydrogen Energy*, 2016, **41**, 21990–21999.

26 M. Wichert, R. Zapf, A. Ziogas, G. Kolb and E. Klemm, *Chem. Eng. Sci.*, 2016, **155**, 201–209.

27 K. Ploner, L. Schlicker, A. Gili, A. Gurlo, A. Doran, L. Zhang, M. Armbrüster, D. Obendorf, J. Bernardi and B. Klötzer, *Sci. Technol. Adv. Mater.*, 2019, **20**, 356–366.

28 N. Köwitsch, L. Thoni, B. Klemmed, A. Benad, P. Paciok, M. Heggen, I. Köwitsch, M. Mehring, A. Eychmüller and M. Armbrüster, *ACS Catal.*, 2020, **11**, 304–312.

29 L. Thoni, N. Metzkow and A. Eychmüller, *J. Sol-Gel Sci. Technol.*, 2023, **107**, 218–226.

30 O. Martin, A. J. Martín, C. Mondelli, S. Mitchell, T. F. Segawa, R. Hauert, C. Drouilly, D. Curulla-Ferré and J. Pérez-Ramírez, *Angew. Chem.*, 2016, **128**, 6369–6373.

31 M. S. Frei, C. Mondelli, A. Cesarini, F. Krumeich, R. Hauert, J. A. Stewart, D. Curulla Ferré and J. Pérez-Ramírez, *ACS Catal.*, 2019, **10**, 1133–1145.

32 P. Schühle, M. Schmidt, L. Schill, A. Riisager, P. Wasserscheid and J. Albert, *Catal. Sci. Technol.*, 2020, **10**, 7309–7322.

33 K. Lau, P. Schühle, S.-X. Liang, F. de Kock, J. Albert and S. Reichenberger, *ACS Appl. Energy Mater.*, 2021, **4**, 9206–9215.

634 | *React. Chem. Eng.*, 2026, **11**, 625–635

This journal is © The Royal Society of Chemistry 2026

34 P. Schühle, S. Reichenberger, G. Marzun and J. Albert, *Chem. Ing. Tech.*, 2021, **93**, 585–593.

35 R. Stöber, F. Seidl, E. Hoffmann, P. Wasserscheid and P. Schühle, *Sustainable Energy Fuels*, 2024, **8**, 1740–1749.

36 A. Avril, C. Hornung, A. Urban, D. Fraser, M. Horne, J.-P. Veder, J. Tsanaktsidis, T. Rodopoulos, C. Henry and D. Gunasegaram, *React. Chem. Eng.*, 2017, **2**, 180–188.

37 C. H. Hornung, X. Nguyen, A. Carafa, J. Gardiner, A. Urban, D. Fraser, M. D. Horne, D. R. Gunasegaram and J. Tsanaktsidis, *Org. Process Res. Dev.*, 2017, **21**, 1311–1319.

38 M. Kundra, B. Bin Mohamad Sultan, D. Ng, Y. Wang, D. L. J. Alexander, X. Nguyen, Z. Xie and C. H. Hornung, *Chem. Eng. Process.*, 2020, **154**, 108018.

39 M. Kundra, T. Grall, D. Ng, Z. Xie and C. H. Hornung, *Ind. Eng. Chem. Res.*, 2021, **60**, 1989–2002.

40 S. Razza, T. Heidig, E. Bianchi, G. Groppi, W. Schwieger, E. Tronconi and H. Freund, *Catal. Today*, 2016, **273**, 187–195.

41 C. Busse, H. Freund and W. Schwieger, *Chem. Eng. J.*, 2024, **489**, 151139.

42 L. Eckendörfer, D. Rudolf, A. Brix, M. Börnhorst and H. Freund, *Annu. Rev. Chem. Biomol. Eng.*, 2024, **15**, 163–186.

43 Y. Zhu, B. Bin Mohamad Sultan, X. Nguyen and C. Hornung, *J. Flow Chem.*, 2021, 1–9.

44 D. Arora, M. Richards, Y. Zhu, I. Martinez-Botella, X. Wang, Z. Xie, J. Chiefari, S. Saubern and C. Hornung, *Chem. Eng. Process.*, 2024, **201**, 109822.

45 T. Solymosi, F. Auer, S. Dürr, P. Preuster and P. Wasserscheid, *Int. J. Hydrogen Energy*, 2021, **46**, 34797–34806.

46 P. Nathrath, Y. R. Ramzi, M. Bierling, S. Thiele, P. Wasserscheid and P. Schühle, *Catal. Sci. Technol.*, 2024, **14**, 980–989.

47 M. C. Biesinger, *Converting From Atomic Percent to Weight Percent and Vice Versa*, 2021, https://www.xpsfitting.com/search/label/Atomic%20and%20Weight%20%25%20Converter).

48 E. Tronconi and G. Groppi, *Chem. Eng. Technol.*, 2002, **25**, 743–750.

49 J. Han, X. Wang, X. Jin, R. Legg, M. Mayyas, C. Hornung and C. Doblin, *Int. J. Hydrogen Energy*, 2025, **158**, 150440.

This journal is © The Royal Society of Chemistry 2026

React. Chem. Eng., 2026, **11**, 625–635 | **635**